Special Feature: Design of High-power Lithium-ion Batteries with Long Operational Life

Research Report

Multiscale Simulations of a Li Diffusion in Lithium-ion Batteries

Nobuko Ohba, Shunsuke Yamakawa and Ryoji Asahi

Report received on Aug. 1, 2017

ABSTRACT Diffusion of Li ions is an elementary process in lithium-ion batteries (LIBs), because it is correlated to power performance of the charging/discharging speed of LIBs. In order to reveal the dynamics of Li ions in the diffusion mechanism, atomic scale and mesoscale simulations for the respective negative and positive electrodes have been conducted.

A hybrid quantum-classical simulation method is applied to atomic-scale simulation in order to be able to consider the deformation of the C layers of graphite, which is used as a negative electrode material. The concentrated Li ions in the same intraplane of C layers are scattered isotropically in the layer due to their mutual Coulomb repulsive interaction. After the total system is thermalized well, the cage structure in which some Li ions cohere appears. Diffusivity of Li ions inside the cage is much higher than that of the cage itself. The long-term diffusion constant of the cage is of the same order as that of an isolated Li ion in graphite.

Layered Li transition-metal oxides such as $LiCoO_2$ are widely used as active materials for the positive electrode of LIBs. In order to gain a quantitative understanding of the effect of the microstructure in the electrode, phase-field models for non-Fickian Li diffusion in two-dimensional polycrystalline microstructures have been developed. The calculation results suggest that both the inter-granular angle mismatch and the grain boundary diffusivity are crucial parameters for evaluating the apparent discharge property at a high discharge rate. If we can experimentally evaluate the grain size relative to the electrode size from a two-dimensional image, we can roughly predict discharge properties and suggest a microstructure for optimizing the electrode performance.

As demonstrated, these multiscale simulations are powerful tools for understanding Li-transport properties in depth, and thus for designing better electrodes in batteries.

KEYWORDS Li-ion Diffusion, Li-ion Rechargeable Battery, Hybrid Simulation, Molecular Dynamics, Density-functional Theory, Phase-field Model, Polycrystalline Microstructure, Elastic Strain

1. Introduction

Batteries that meet the demands of high energy storage and high power are required for applications in vehicles. Lithium-ion batteries (LIBs) have attracted increased attention recently as high-performance secondary batteries. In a LIB, charging and discharging are conducted by moving Li ions into the electrolytes between the positive and negative electrodes. Various materials can be used as an electrode or electrolyte. A typical LIB is composed of nonaqueous electrolytes such as organic solvents, carbon materials such as the graphite anode, and Li transition metal oxide for the positive electrode. The diffusivity of Li ions in such materials and their interface relates to the power performance of the charging/discharging speed of LIBs. Reduction of the transfer resistance of Li ions is needed in order to improve input and output characteristics. Therefore, understanding the diffusion mechanism is important in the development of LIBs.

There exist various simulations for analyzing the transport properties of Li ions into each constituent material of LIB. In the combined simulation of quantum chemical calculations and the classical molecular dynamics (MD) simulations for the organic solvent of electrolyte liquid reported by Oleg et al.,[(1)] transporting properties of Li ions and their solvate were investigated.

In the case of simulating the diffusivity of Li ions in a graphite anode, it is necessary to take into

© Toyota Central R&D Labs., Inc. 2017

consideration the structural changes due to expansion of the interlayer of graphite caused by the inserted Li ions. The hybrid quantum (QM)-classical (CL) simulation[2,3] with the buffered-cluster method (BCM),[4] which is one of the multiscale simulation methods applicable to such a long-ranged stress field, has been developed. It has been applied to the thermal diffusion process analysis of a single Li atom in graphite at the diluted limit of the Li concentration.[5,6] Moreover, an O(N) type Real-space Grid based Density Functional Theory (RGDFT) code has also been developed[7] and the Li-ion transfer mechanism through the solid-electrolyte interface (SEI) is analyzed by the 2400-atom first-principles molecular dynamics simulation.[8]

On the other hand, the diffusivity of Li ions in a positive electrode material such as Li transition metal oxide depends on the orientation of the crystal. In addition, a positive electrode is polycrystalline and the grain boundary (GB) has an influence on the Li diffusion. Thus, an application of the calculation technique such as the phase-field model reflected on the microstructure of the materials is effective.

In this study, the diffusivity of Li ions in negative and positive electrodes is analyzed by an atomic-nano-scale simulation and microscopic materials structure scale simulation, respectively. This paper is organized as follow: The hybrid QM-CL simulation investigation and results of the diffusion process of multiple Li atoms with both the intraplane and interlayer interaction of Li ions are given in Sec. 2. In Sec. 3, phase-field simulation is conducted in order to clear the discharge properties of the polycrystalline Li transition metal oxide of $LiCoO_2$ in relation to the crystal anisotropy, grain size, GB diffusivity, and elastic stress field associated with Li intercalation. A summary is given in Sec. 4.

2. A Hybrid Quantum Classical Simulation on the Diffusivity of Li Atoms in the Graphite

In the hybrid QM-CL simulation, Li atoms and those surrounding C atoms were set as the QM region, and this region was embedded in the classical system described in the empirical interaction model. The buffered cluster method (BCM)[4] was used as the model of the QM-CL boundary. In contrast to the link-atom method,[9] the BCM has universality in materials and a QM-region shape, and is thus suitable for problems with a moving QM region. The details of the calculation conditions are described in Refs. (10), (11), (12) and (13).

2. 1 Intraplane Interaction among Li Ions

A simulation model shown in **Fig. 1** contains a 9-layer graphite structure consisting of 12096 C atoms and 7 Li atoms and utilizes periodic boundary conditions. The simulation temperature T was set to be 443 K. The inter-layer direction of graphite and its perpendicular plane are the z-axis and the x-y plane, respectively. The system size was (L_x, L_y, L_z) = (59.57,58.96,30.58) Å. All Li atoms existed in the same layer, so in this case the in-plane interaction among Li atoms was considered. The structure of the graphite-layer with inserted Li atoms was set as AA-stacking, and that without Li was AB-stacking. In order to investigate the effects of the inter-layer interaction of Li, we also conducted the simulation with the Li atoms arranged in the inter-layer direction next to each other.

First, 7 Li atoms were placed in the adjacent six-membered ring in the same layer of graphite so as to consider the in-plane interaction effects for the diffusivity of Li ions. When Li atoms are located close to each other, quantum mechanical interaction between Li cannot be ignored, so a large QM region must be set in order to include all Li atoms and their surrounding C atoms. On the other hand, when the distance between Li atoms is sufficiently far and each Li is isolated, QM-calculation is conducted independently in each region. In this case, only the interaction through the mechanical bonding in the CL region needs to be taken into account. From the preliminary calculation results of the forces acting on Li ions, we estimated

Fig. 1 Simulation model viewed from y-direction. Blue, bright gray, and gray spheres denote Li, QM-C, and CL-C atoms, respectively.

© Toyota Central R&D Labs., Inc. 2017

that the required distance between Li atoms for it to be considered a QM region was 10 Å.

The snapshots of the diffusion process of Li at simulation time t = 0, 0.5, 2.5 and 5.0 ps are shown in **Fig. 2**. The majority of the valence electrons of the Li atoms are transferred to the surrounding C atoms, and as a result, the Li has a positive charge in the graphite layers, being a Li^+ ion.(5) Therefore Li ions were scattered isotropically by their Coulomb repulsive interaction in the early stages of diffusion. The QM region was selected adaptively following the movement of the Li ions. Thus, there were four independent QM regions at t = 5 ps in Fig. 2. The Li underwent movement in the thermal diffusion mode after around 0.5 ps, at which time the Li ions were widely separated. Then the diffusivity of Li became relatively slow, and the Li ions diffused in a limited area. **Figure 3** expresses the distribution of the inter-layer distance (d) of the upper and lower graphene sheets where Li atoms existed after 2.5 ps in this hybrid simulation. The inter-layer distance is shown by the color of each C atom in Fig. 3. In this simulation, the inter-layer distances are around 4.0 Å with Li and 3.6 Å without Li. The inter-layer distance of the graphite domain where the Li ions exist is greater than that in the domain with no Li at every simulation time; that is, the graphene sheets create the cage confining the movement of Li atoms and the Li ions diffuse in the limited area in the cage.

The time evolution of average values of the expanse from the center-of-mass of 7 Li atoms is shown in **Fig. 4**. This value was regarded as the radius of the cage, and it was estimated as almost 13.5 Å after a time step of 11 ps.

The red line in **Fig. 5** shows the mean square displacement of the average of 7 Li atoms. The mean square displacement of a single Li atom existing in the graphite is also shown with a blue line. It is clear that the multiple Li ions diffuse well compared with the diffusion of the single Li atom in the graphite. We think the reason for this situation is the correlation of the Li diffusion in graphite and the interlayer distance as reported in Refs. (5) and (6). The interlayer distance of graphite around the Li remains about 4.0 Å in this simulation. It is too great a distance for Li ions to be trapped in the graphite layer. The presence of multiple Li atoms expands the elongated interlayer distance region. Namely, the cage becomes larger than that in

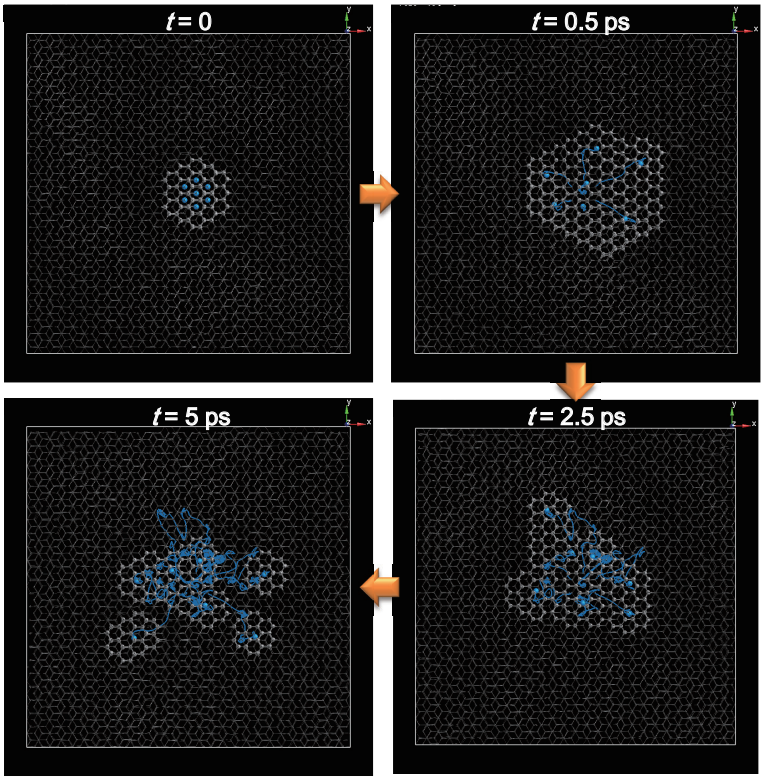

Fig. 2 Snapshots at simulation times of t = 0, 0.5, 2.5, and 5 ps. Brightness region is QM-region, and blue and gray spheres are Li and C atom, respectively. The blue line shows the trajectory of Li atoms.

© Toyota Central R&D Labs., Inc. 2017

the single Li case, and an individual Li ion diffuses well in the expanded cage.

The mean square displacement of the center-of-mass (COM) of 7 Li atoms is plotted with a magenta line in Fig 5. The diffusivity of COM was the same as that for a single Li atom. Therefore, Li ions diffuse well only in the limited region (inside the cage) generated by multiple Li atoms. From the simulation of only one Li atom existing in graphite, a small cage was observed. Its interlayer distance within the cage was about 4.0 Å, which was the almost same value as that in the case of 7 Li atoms. The interlayer distance around the cage was roughly estimated to be less than 3.6 Å in both cases. Therefore, stretching the interlayer distance to the same degree is needed for the cage itself to move, in cases of either one Li or 7 Li atoms. In other words, it is thought that the diffusivity of the cage (COM) including 7 Li atoms is as slow as that of one Li atom. The mass effect may provide the suppression of longer-term diffusion of COM in Fig. 5, because the number of atoms included in the cage of multiple Li atoms is larger than that of a single Li atom. Longer-term simulation and much more sampling data will be desired in order to support such a tendency.

Next, the Li atoms were set in the same order as the C_6Li concentration. **Figure 6** shows the diffusion process of Li ions. In the case of C_6Li, Li diffused thermally from the initial setting, since the distance between Li ions was 4.2 Å and the Coulomb repulsion effect was screened well by graphite. On the other hand, there existed the cage effect because the Li atoms diffused in a limited area, which was similar to the former case.

Figure 7 shows the time evolutions of mean square displacement of the Li ions in two cases and in the single Li case. Here, the case illustrated in Fig. 2

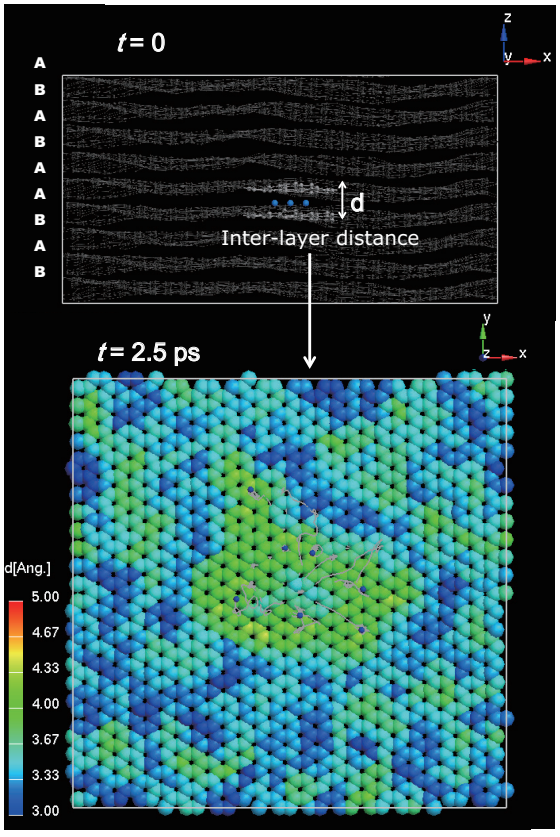

Fig. 3 Atomic inter-layer distance (d) distribution of graphite in *x*-*y* plane at $t = 2.5$ ps. The small spheres show Li atoms and their trajectories are shown as a gray line. The interlayer distance is shown by the color of each C atom (large sphere).

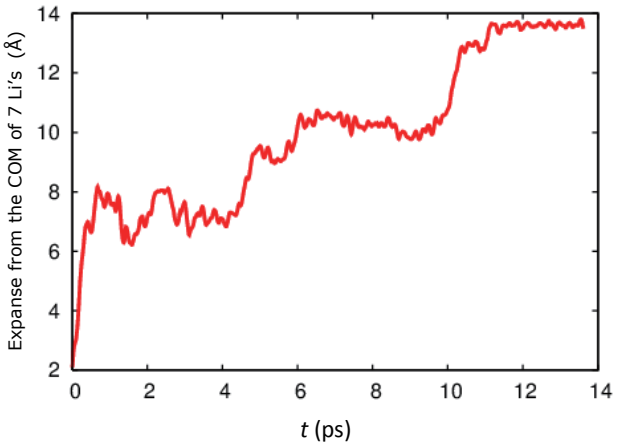

Fig. 4 Time evolution of the average value of the expanse from the center-of-mass (COM) of 7 Li atoms.

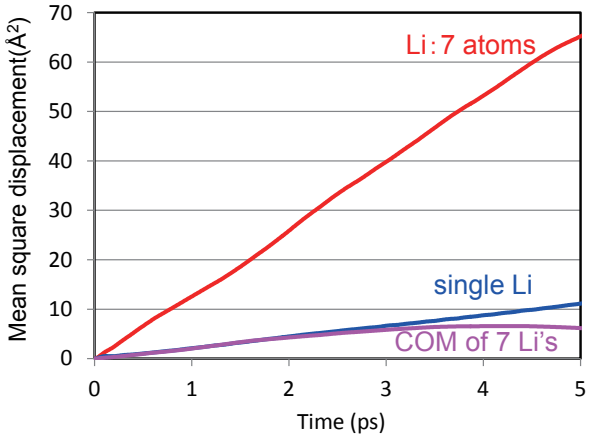

Fig. 5 Time evolution of the mean square displacement.

© Toyota Central R&D Labs., Inc. 2017

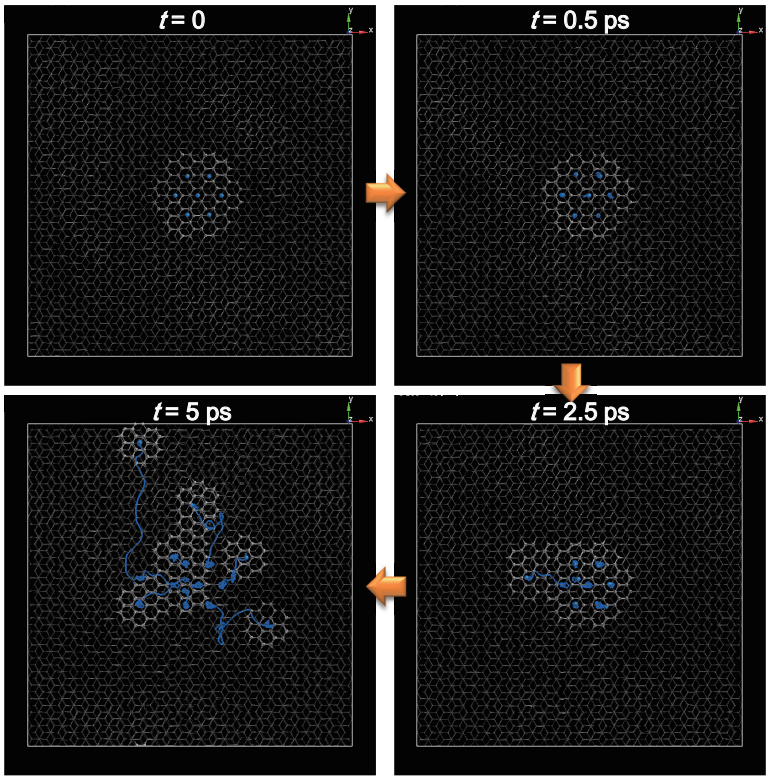

Fig. 6 Snap shots at simulation times t = 0, 0.5, 2.5, and 5 ps in a C_6Li concentration arrangement. The brightness region is a QM-region, and the blue and gray spheres are Li and C atom, respectively. The blue line shows the trajectory of Li atoms.

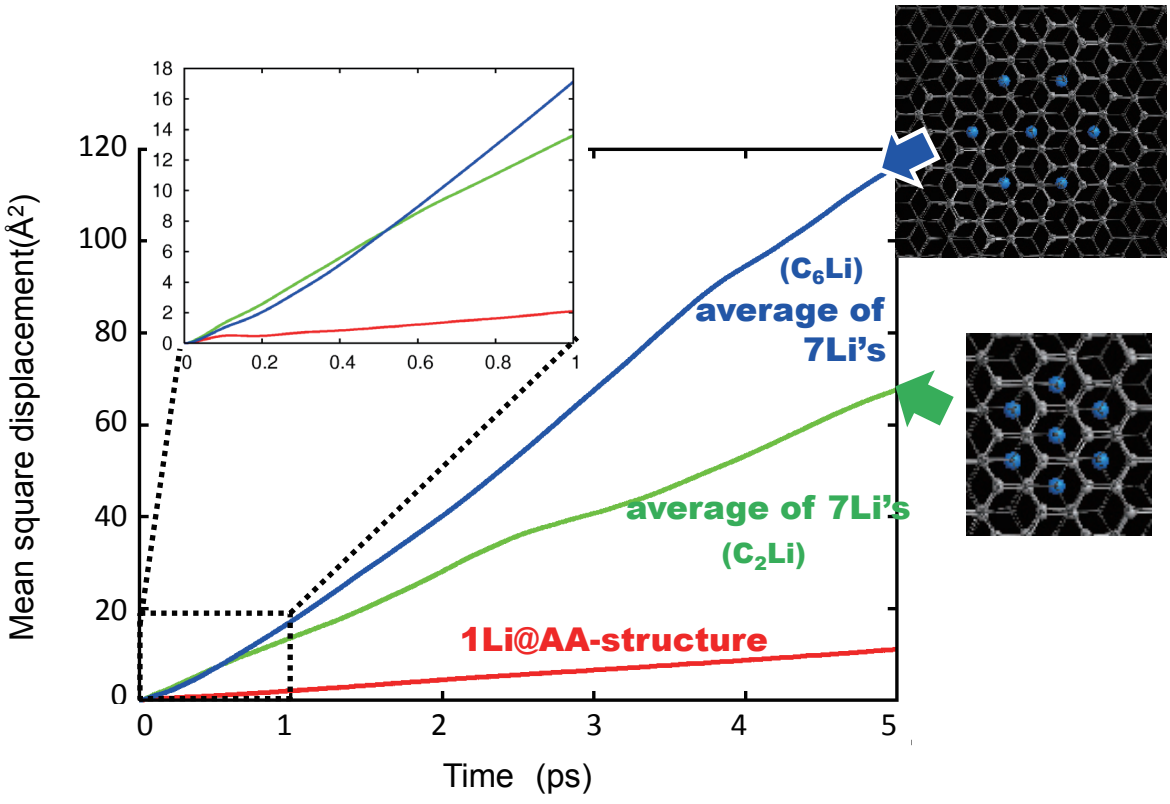

Fig. 7 Time evolution of the mean square displacement. The inserted figure shows the enlarged 0–1 ps.

© Toyota Central R&D Labs., Inc. 2017

is denoted as a C_2Li case since the initial setting of Li atoms corresponds to the C_2Li concentration. In a very short time, the displacement of the C_2Li case was greater than that of the arrangement in the C_6Li concentration, because a Coulomb repulsive effect of around 0.5 ps remained. However, this effect did not extend for a long time (distance), and the mean square displacement in the C_6Li case at 5 ps was rather high compared to that in the C_2Li case. If the system is thermalized well, the diffusivity in the C_6Li and C_2Li case will be to the same degree. Longer-term simulations will be needed for the quantitative estimation of the diffusion coefficient in both cases.

2. 2 Interplane Interaction among Li Ions

In order to investigate the interlayer interaction effects among Li atoms, a hybrid QM-CL simulation run was conducted for 14 Li atoms in 10 layers of graphite. The simulation model is shown in **Fig. 8**. The Li ions were divided into two parts in the graphene sheet. The stacking structure of the graphene layer was set as AA-stacking in which there were Li ions. **Figure 9** depicts the trajectories of Li ions after 3.4 ps. The upper and lower Li ions moved in opposite directions. The trajectories of the Li ions in the upper layer (magenta lines) were separated from those of the Li ions in the lower layer (cyan line) mainly due to the repulsive interlayer interactions of Li. The cage formation, which expands interlayer distance, also stabilizes such a domain separation. This result suggests the origin of the formation of the staging structure in the Li-graphite intercalation compounds where the repulsive interaction between Li ions alternately stabilizes the layers with and without Li.

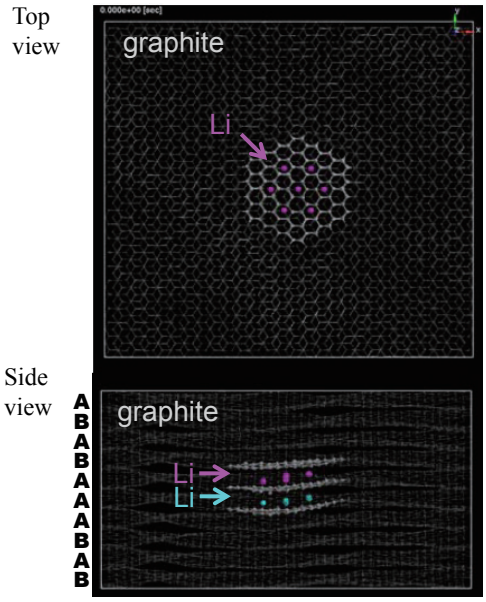

Fig. 8 Top view and side view of the simulation model. Magenta, cyan, bright gray, and gray spheres denote Li in the upper layer, Li in the lower layer, QM-C, and CL-C atoms, respectively.

3. Effects of Microstructure on Apparent Li Diffusivity of Polycrystalline $LiCoO_2$

The most commonly used active materials for the positive electrode in LIBs are layered Li oxides, namely transition-metal oxides that are characterized by two-dimensional (2D) Li diffusion paths.[14-17] A typical electrochemical reaction[18] occurring in the Li oxides is represented by Eq. (1):

$$\mathrm{Li\,MO_2} \underset{\text{Discharge}}{\overset{\text{Charge}}{\rightleftarrows}} \mathrm{Li_{1-x}\,MO_2} + x\,\mathrm{Li^+} + xe^- . \quad (1)$$

In particular, $LiCoO_2$ is the most basic layered Li oxide, and its crystal structure[19] is represented in **Fig. 10**. The atomic diffusivity in a layered material depends on its crystallographic orientations. In the case of $LiCoO_2$, the self-diffusion coefficient of Li in the direction perpendicular to the basal plane, $D_{\mathrm{self\_}c\mathrm{\_axis}}$, is smaller than that in the direction along the basal plane of the hexagonal structure, $D_{\mathrm{self\_basal}}$, by at least one order of magnitude.[20] Experimental observation has revealed that a high-coincidence

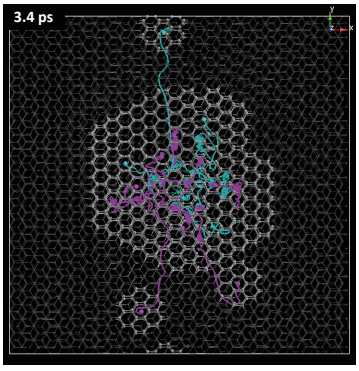

Fig. 9 The trajectories of Li atoms after 3.4 ps. The magenta and cyan lines denote the trajectories of Li in the upper and lower layer, respectively.

© Toyota Central R&D Labs., Inc. 2017

twin boundary stably exists in $LiCoO_2$ thin films.[21] Therefore, the disconnectedness of the intergranular diffusion paths is believed to restrict the Li flux in an actual polycrystalline $LiCoO_2$ film. As a result, microstructural inhomogenities such as crystal anisotropy, grain size, and grain boundary (GB) can limit the transport properties of Li.

In order to fabricate materials with improved performances, an understanding of the properties that contribute to the performance of LIBs is necessary. The rational design of Li-based active materials with better performance cannot proceed without an accurate and detailed comprehension of the Li-ion conduction mechanism at the nanometer to micrometer levels. Nevertheless, since there are difficulties involved in the experimental assessment of the conduction mechanism and most numerical simulations have adopted an isotropic diffusion medium,[22,23] the effect of the microstructure on Li-ion conduction is yet to be clearly and completely understood. In the present study, we concentrate on investigating the discharge properties of polycrystalline $LiCoO_2$ in relation to the crystal anisotropy, grain size, GB diffusivity, and elastic stress field associated with Li intercalation.

The phase-field method,[24,25] which is a continuum model and obeys local thermodynamic equilibrium, was adopted to investigate Li diffusion in randomly oriented polycrystalline $LiCoO_2$. The diffusion phenomenon was calculated based on the Gibbs free energy of the binary solution in the Li-vacancy system,

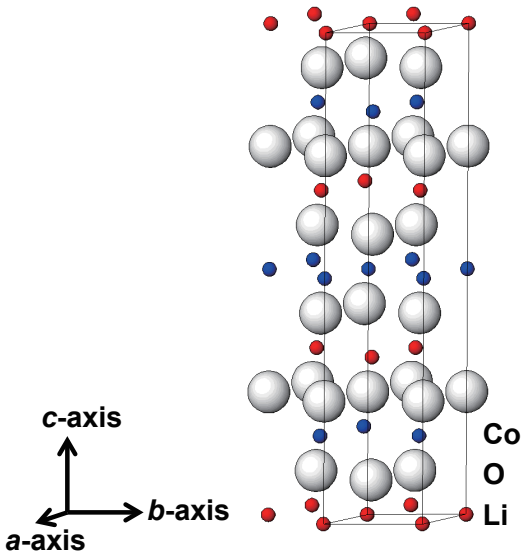

Fig. 10 Crystal structure of $LiCoO_2$.

which was derived from the experimental or theoretical open-circuit potential of Li_xCoO_2 and the elastic strain energy associated with Li intercalation–deintercalation. Furthermore, the model incorporated the Butler–Volmer equation to determine the Li flux across the $LiCoO_2$–electrolyte interface. Information obtained from the model on the crucial aspects of anisotropic materials can be used to quantitatively understand their Li-transport properties, thus allowing the facilitation of topotactic electrochemical reactions for high-power applications.[26]

3. 1 Methods of Calculation

3. 1. 1 Formulation

The temporal evolution of the Li concentration arising from the non-Fickian Li diffusion in an anisotropic diffusion media is solved by numerically calculating the following Cahn–Hilliard diffusion equation in combination with the anisotropic self-diffusion tensor:

$$\frac{\partial c}{\partial t} = \nabla \cdot \left[\frac{c(1-c)}{RT} \left(\mathbf{D}' \nabla \frac{\delta G_{\text{system}}}{\delta c} \right) \right], \tag{2}$$

where c is the Li concentration ratio ranging from 0 to 1, R is the gas constant, and T is the absolute temperature. The effect of the polycrystalline microstructure on the Li diffusivity is considered through the diffusion tensor, $\mathbf{D}'$, by correlating it with the orientation angle of each grain in the following form:

$$D'_{ij} = A_{im} A_{jn} \delta_{mn} D_{mn}, \tag{3}$$

where A_{im} is the rotation matrix randomly allocated to each crystal grain, and δ_{mn} is the Kronecker delta. We assume isotropic Li diffusion on the basal plane of $LiCoO_2$, with D_{11} (= D_{22}) and D_{33} corresponding to $D_{\text{self\_basal}}$ and $D_{\text{self\_}c\text{\_axis}}$, respectively. The total free energy of the bulk system, G_{system}, is assumed to be the volume integral of the well-defined local free-energy density over the entire volume, V:

$$G_{\text{system}} = \frac{1}{V} \int_{\mathbf{r}} \left(G_{\text{chem}} + E_{\text{grad}} + E_{\text{str}} \right) \mathrm{d}\mathbf{r}, \tag{4}$$

© Toyota Central R&D Labs., Inc. 2017

where G_{chem}, E_{grad}, and E_{str} correspond to the chemical free energy, gradient energy, and elastic strain energy, respectively. Here, G_{chem} refers to the uniform binary solution in the Li-vacancy system. In a solid-solution system such as that of Li_xCoO_2, E_{grad} has no significant effect on the temporal evolution of Eq. (2). E_{str} is expressed in the following form:[27]

$$E_{str} = \frac{1}{2} C_{ijkl} \left(\varepsilon_{ij}^{c} - \varepsilon_{ij}^{0} \right) \left(\varepsilon_{kl}^{c} - \varepsilon_{kl}^{0} \right), \quad (5)$$

where C_{ijkl} is the elastic stiffness constant. The elasticity of $LiCoO_2$ is presumed to be isotropic, and thus the corresponding stiffness component is defined by two parameters called Lamé's constants, λ and μ. The variables ε_{ij}^{c} and ε_{ij}^{0} are the constrained strain and the eigenstrain, respectively, and they are expressed as follows:

$$\varepsilon_{ij}^{c} = \bar{\varepsilon}_{ij}^{0} + \delta\varepsilon_{ij}^{c}, \quad (6)$$

$$\varepsilon_{ij}^{0} = A_{im} A_{jn} \eta_{mn}, \quad (7)$$

where η_{mn} is the lattice misfit, $\bar{\varepsilon}_{ij}^{0}$ is the mean strain averaged over the entire system, and $\delta\varepsilon_{ij}^{c}$ is the deviation of the local strain from $\bar{\varepsilon}_{ij}^{0}$. $\delta\varepsilon_{ij}^{c}$ is calculated using a self-consistent iterative scheme in the Fourier space.[28]

3. 1. 2 Numerical Calculation

The effect of various microstructures on the discharge property was evaluated in combination with the Li diffusion–electrochemical-reaction model and the two-dimensional microstructure, with the crystallographic *c* axis of each crystal grain included in this plane. The plane strain condition was assumed. **Figure 11** shows the microstructural features considered in this model with the crystal structure of $LiCoO_2$. We assumed that the GB is a thin layer between neighboring grains. Fisher et al.[21] evaluated the activation energy of Li diffusion at the twin boundary core by using first-principles calculation, and they obtained a value almost twice as large as that in the single crystal. The GB width was set to 2 nm, which approximately corresponds to the width of the region where the activation energy deviates from that inside the grain. D_{self_basal} and $D_{self\_c\text{-}axis}$ of the inner grains were calculated to be 1.0×10^{-9} and 1.0×10^{-11} $cm^2 \cdot s^{-1}$, respectively.[20,29] The Li diffusivities along and across the GB thin layer, $D_{gb//}$ and $D_{gb\perp}$, are defined as $D_{gb//} = D_{self\_basal}$ and $D_{gb\perp} = 0.01 D_{self\_basal}$, respectively. **Figure 12** shows the two-dimensional polycrystalline microstructures generated from multi-phase-field simulations,[30] where the *y*-axis is parallel to the global direction of Li transport. To assess the influence of the connectivity of the conduction path between the crystal grains on the Li diffusivity, in our paper,[24] the area-averaged value was evaluated using the following equation to take into account the relative orientation between neighboring grains:

$$\theta_{relative} = 90 - \sum_{n_y=1}^{n_y=n_{y\_max}} \left| \sum_{n_x=1}^{n_x=n_{x\_max}} \left[90 - \theta\left(n_x, n_y\right) \right] \right| / \left(n_{x\_max} \times n_{y\_max} \right), \quad (8)$$

where n_{x_max} and n_{y_max} denote the number of grid points along the *x*-axis and *y*-axis, respectively, in the numerical simulation region. The fine- and coarse-grained microstructures with a median, lower and upper limit of $\theta_{relative}$ were studied. As listed in **Table 1**, it is confirmed that the apparent Li diffusivity decreases as $\theta_{relative}$ increases. The number of grid points along each axis was set to be 256; the grid spacing was 0.02 μm. Finer grid spacing near the GBs was used to represent Li diffusion in the GB thin layer. Based on previously reported theoretical estimates,[31]

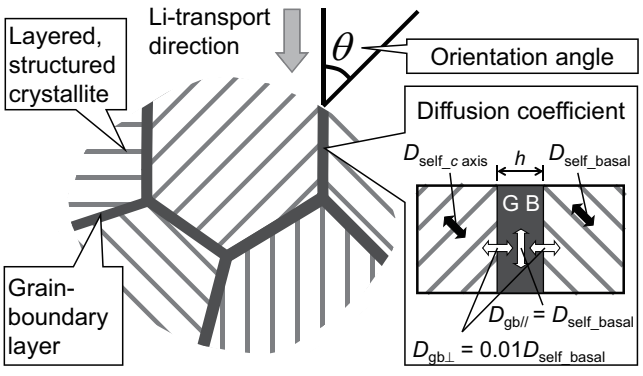

Fig. 11 Schematic illustration of the microstructural characteristics treated in this simulation.

© Toyota Central R&D Labs., Inc. 2017

the values of λ and μ were set to 133.5 and 120.9 GPa, respectively. When a Li atom is deintercalated from the host lattice, the lattice constant along the c axis increases locally owing to the electrostatic repulsion of the oxygen layer.[32] Therefore, it was assumed that the crystal lattice misfit can be expressed as $\eta_{ij} = (1-c)\delta_{ij}\eta'_{ij}$, where the coefficient δ_{ij} is the Kronecker delta. Based on previously reported lattice parameters measured from X-ray diffraction patterns,[33,34] the values of η'_{11} $(=\eta'_{22})$ and η'_{33} were set to −0.005 and 0.05, respectively.

To capture the discharge capacity under realistic discharge conditions, the Li flux across the $LiCoO_2$–electrolyte interface was determined by using the Butler–Volmer equation. The interface was set at $y = 0$ and $y = L$, where L represents the length of the simulation region. The equilibrium potential of $LiCoO_2$ as a function of Li concentration was adopted.[35] The initial voltage was set to 4.026 V, which corresponds to a Li concentration of 0.6 at equilibrium. The

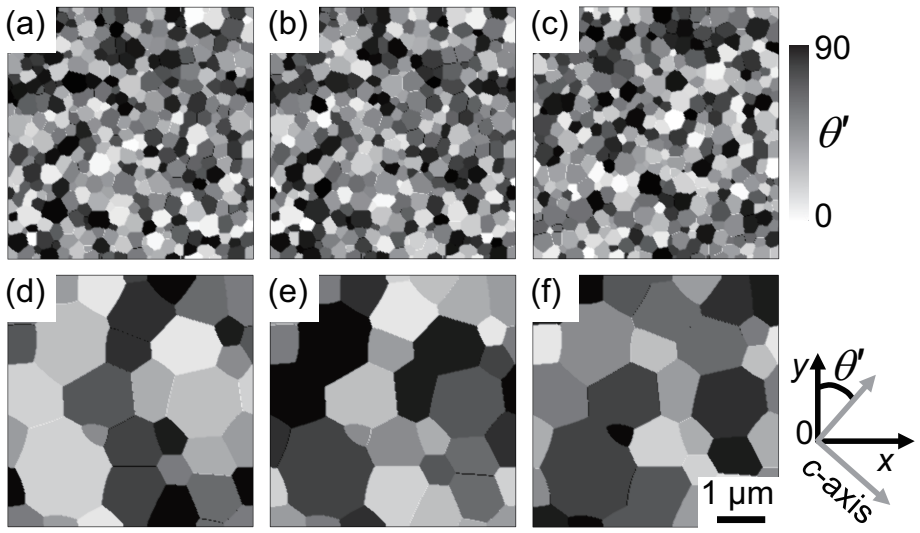

Fig. 12 Two-dimensional models of a polycrystalline microstructure with randomly oriented grains. The orientation angle of each grain is represented by its gray tone. The variable is defined as $\theta' = 90 - |90 - \theta|$. The orientation angle θ assigned to each grain is between zero and 180°. The manners of the assignment of the orientation angle are chosen such that the resultant $\theta_{relative}$ values defined in Eq. (8) correspond to lower limit ((a) and (d)), median ((b) and (e)), and upper limit ((c) and (f)).

Table 1 Apparent diffusion coefficient of Li. The value of $\theta_{relative}$ is defined in Eq. (8). Parentheses denote the relative ratio, calculated with the E_{str} either omitted or included.

Model	$\theta_{relative}$ (°)	D_{app} ($\times 10^{-9}$ cm^2 s^{-1})			
		$D_{gb//} = D_{self\_basal}$		$D_{gb//} = 0.01D_{self\_basal}$	
		E_{str} is omitted	E_{str} is included	E_{str} is omitted	E_{str} is included
Fine-grained					
(a)	75.1	1.49	1.57 (1.05)	0.44	0.46 (1.05)
(b)	79.2	1.51	1.59 (1.05)	0.44	0.46 (1.05)
(c)	83.3	1.29	1.36 (1.05)	0.39	0.41 (1.05)
Coarse-grained					
(d)	63.6	1.29	1.42 (1.10)	0.78	0.85 (1.09)
(e)	71.9	1.05	1.09 (1.04)	0.61	0.64 (1.05)
(f)	79.8	0.62	0.66 (1.06)	0.39	0.41 (1.05)

© Toyota Central R&D Labs., Inc. 2017

kinetic rate constant of the electrochemical reaction was 2.0×10^{-6} $cm^{5/2} \cdot mol^{-1/2} \cdot s^{-1}$. The current density for this reaction was set to be 3.45 $mA \cdot cm^{-2}$, which corresponds to a discharge rate of approximately 20C. The temperature was set at 298.15 K. Since the focus of this study is to derive the relationship between various microstructural features and the constant-current discharge properties of $LiCoO_2$, the model did not explicitly treat the potential distribution in $LiCoO_2$ and the electrolyte, or the mass transport of Li ions in the electrolyte.

3. 2 Results and Discussion

The effects of microstructure on the apparent diffusion coefficient and discharge properties were investigated; the results are discussed in the following sections.

3. 2. 1 Apparent Diffusion Coefficient

Figure 13 shows a schematic illustration of the oriented-single-crystal model. The Li composition was $x = 1.0$ in Li_xCoO_2, and the stress was assumed to have a value of 0. Since there was no constraint to the distortion of the entire body, the stress remained at zero when the Li composition was varied very slowly from 1.0 to 0.6. The Li composition of the single crystal interior was lower than that of the electrochemical reaction surface when the potential was increased stepwise from this state. Subsequently, this compositional difference induced an elastic strain in the crystal. Figure 13 also shows the distribution of σ_{xx} at a mean Li concentration of 0.605. As shown in Fig. 13(a), tensile stress was induced in the x direction in the (100)-oriented model, in which the Li layer was parallel to the x axis. The introduction of tensile elastic stress during Li intercalation was experimentally observed in a $LiCoO_2$ thin film with a preferred orientation in the (104) direction, which was obtained from the curvature of the glass substrate detected by the laser beam deflection.[36] Contrary to this, as shown in Fig. 13(b), the compressive stress state was along the x direction in the (003)-oriented model, in which the Li layer was perpendicular to the x axis. Since the misfit strain of the a and b axes was one order of magnitude lower than that of the c axis, the absolute stress value for each model also changed by one order of magnitude. In addition, since there was no concentration gradient in the x direction, the vertical stress in this direction was close to zero in each model.

To clarify whether or not this variation in the elastic stress field affects Li diffusivity, the apparent diffusion coefficient, D_{app}, was estimated. The D_{app} value was calculated from the time-dependent current by mimicking the measurement manner of the potentiostatic intermittent titration technique (PITT).[37] The boundary conditions at $x = 0$ and

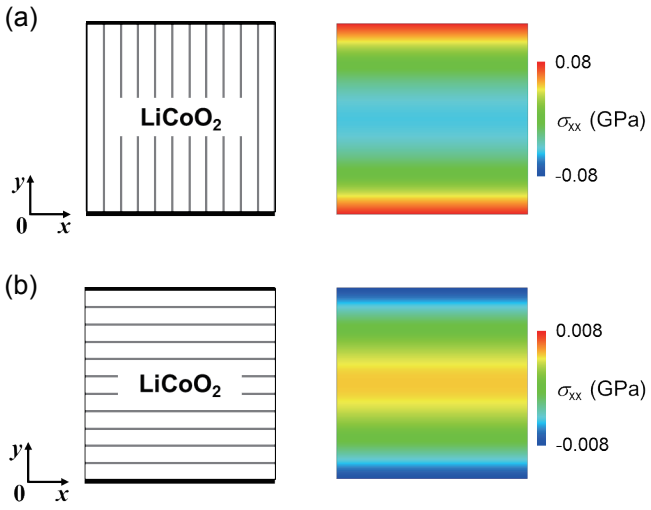

Fig. 13 Schematic illustrations of 2D single-crystal models in which the (a) c axis or (b) a axis is parallel to the x axis. The bold lines located on the upper or lower boundary of the y axis represent the electrochemical interfaces. The figures on the right represent the distribution of σ_{xx} at a mean Li concentration of 0.605.

© Toyota Central R&D Labs., Inc. 2017

$x = L$ were $c_{x=0} = c_{x=L}$, and the potentials at $y = 0$ and $y = L$ were constant. To prevent the surface reaction from becoming a rate-determining step, the kinetic rate constant for the electrochemical reaction was set to 1.0×10^{-3} $cm^{5/2}\cdot mol^{-1/2}\cdot s^{-1}$. A potential step of about 8 mV (from 4.026 to 4.018 V) was applied. The apparent diffusion coefficients of all of the models are shown in **Table 2**.

The diffusion of Li from the electrochemical reaction surface towards the crystal interior was induced along the y direction. Table 2 shows that the D_{app} value of the (100)-oriented model was larger than that of the (003)-oriented model. Although the value obtained by multiplying the eigenstrain by the stress value was included in the Li diffusion potential, $\delta G_{system}/\delta c$, Li diffusion was promoted in directions that reduced the stress gradient by reducing the Li concentration gradient. Therefore, the D_{app} value increased by about 8% in the (100)-oriented model when compared with the case in which the elastic strain energy was not taken into account. In the (003)-oriented model, no significant difference was observed since the misfit of the a axis was small in comparison with that of the c axis.

Table 2 Apparent diffusion coefficients of Li in single-crystal models.

Microstructural model	D_{app} ($\times 10^{-9}$ $cm^2\cdot s^{-1}$)	
	E_{str} is omitted	E_{str} is included
Single-crystal model		
(100)-oriented (Fig. 13(a))	7.06	7.61
(003)-oriented (Fig. 13(b))	0.073	0.073

3. 2. 2 Discharge Properties

Figure 14 shows the constant-current discharge properties in accordance with the corresponding microstructures shown in Fig. 12. The solid and broken lines denote the inclusion and exclusion, respectively, of E_{str}. The simulation results under the conditions of $D_{gb//} = D_{self\_basal}$ and $D_{gb//} = 0.01D_{self\_basal}$ are indicated by the black and blue lines, respectively. The variations in discharge properties with changes in the fine-

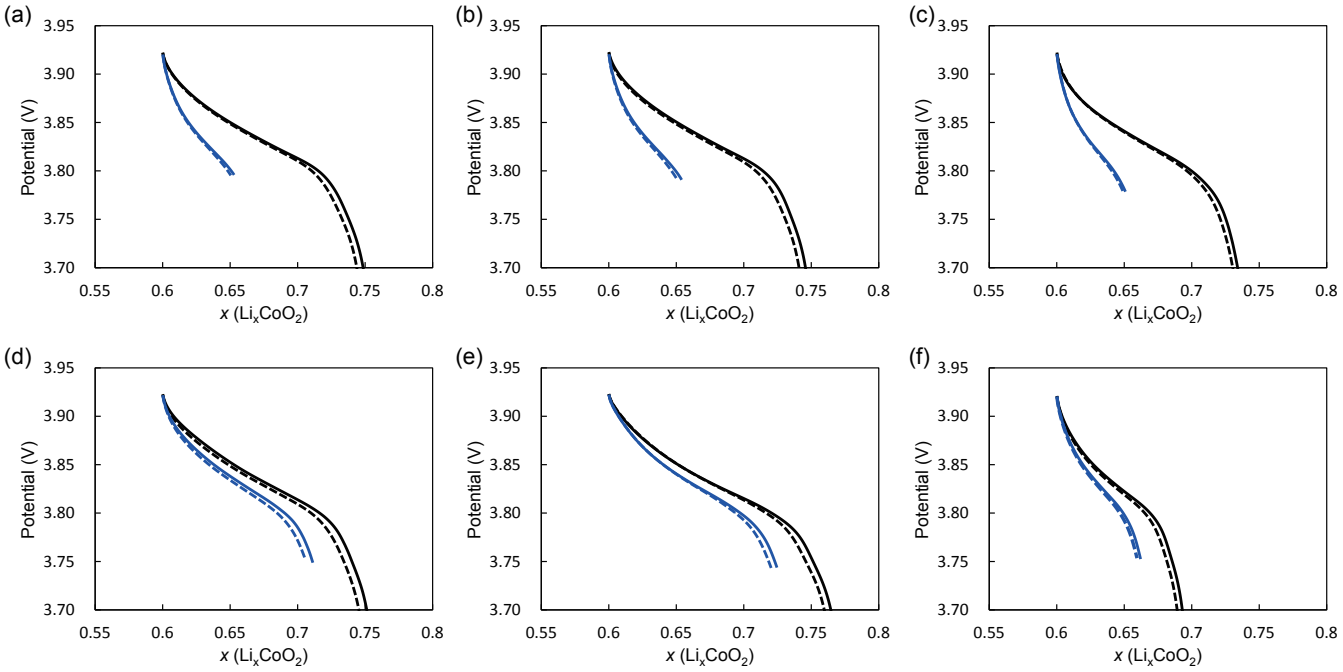

Fig. 14 Constant-current discharge properties at 298.15 K. The current density was fixed at 3.45 $mA\cdot cm^{-2}$. The black and blue lines represent the simulation results obtained under the conditions of $D_{gb} = D_{self\_basal}$ and $D_{gb} = 0.01D_{self\_basal}$, respectively. The solid and broken lines indicate the inclusion and exclusion, respectively, of E_{str}. The labels (a)-(f) correspond to the model (a)-(f) in Table 1.

© Toyota Central R&D Labs., Inc. 2017

grained microstructures were small (Fig. 14(a)-(c)), while variations of the coarse-grained microstructures were larger (Fig. 14(d)-(f)). Li segregation at the electrochemical reaction interface appeared to result in differences in the discharge capacity of each microstructure. The spatial distribution of Li concentration at a mean Li concentration of 0.65 is shown in **Fig. 15**. In the coarse-grained microstructure, the initial assignment of the orientation-angle distribution induced a remarkable variation in Li concentration (Fig. 15(d)-(f)), since the apparent Li diffusivity of the coarse grained model varies widely as shown in Table 1.

Figure 14 shows another important feature, where the discharge capacities of the fine-grained models were smaller than those of the coarse-grained models when the GB served as a diffusion barrier. The effect of the elastic strain energy on the discharge properties was also visible. Since a greater decrease in the elastic stress field occurred in the vicinity of the region where the Li concentration increased, the elastic strain energy slightly decreased the overpotential in the discharge process. Hence, even though the effect of elastic strain energy was weaker than that of the intergranular angle mismatch or GB diffusivity, it led to a nontrivial change in Li diffusivity during discharge. These tendencies suggest that changes in the Li diffusivity directly appear to the overpotential at the high discharge rate of 20C. In addition, the effect of the elastic strain energy may play a larger role when the overall distortion of the diffusion medium is constrained, as observed in the all-solid-state batteries; this condition is a potentially fruitful area of future research. Moreover, to perform more precise and quantitative estimation of the effect of the elastic strain energy, it is necessary to consider the anisotropic elastic constants and estimate the parameters from first-principles calculations.

4. Summary

In order to investigate the diffusivity of Li atoms in the negative and positive electrode in the LIB, we performed hybrid QM-CL simulation at the atomic scale and phase field simulation at the mesoscale, respectively.

The hybrid QM-CL simulations revealed the effects for the diffusivity of the intra- and interplane interaction of Li atoms. The Li ions existing in the same layer kept a certain distance from each other due to their Coulomb repulsion. Thermalized Li ions and surrounding C atoms made a cage by deforming the C layers. The present simulation estimated that the radius of the cage was about 13.5 Å. Li ions moved well in the cage. On the other hand, the diffusivity of the cage was the same order as that of a single Li ion in the graphite. The inter-layer interaction between the Li ions and the deformation of C layers caused the Li ions to repel each other. This result suggests the

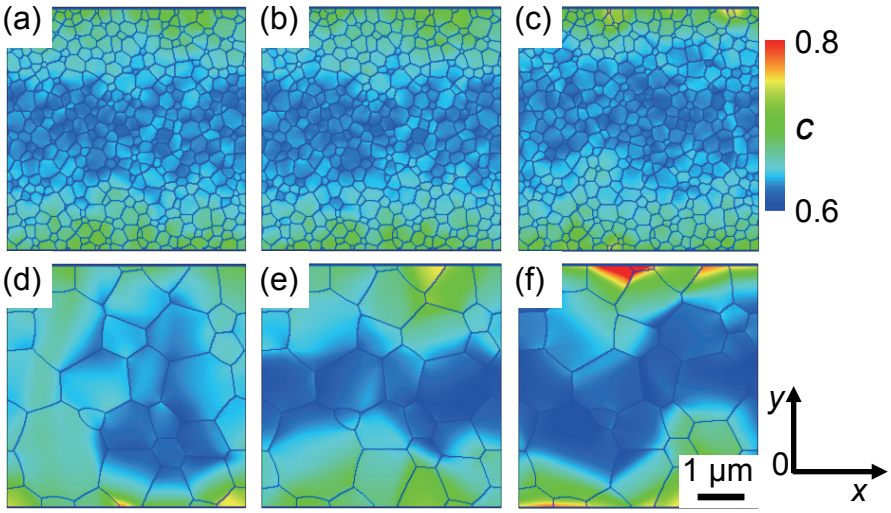

Fig. 15 Distribution of Li concentration during constant-current discharge. The Li-transport direction is parallel to the *y* axis. The mean Li concentration in $LiCoO_2$ is about 0.65. D_{gb} is assumed to be equal to D_{self_basal}; E_{str} is included. The labels (a)-(f) correspond to the model (a)-(f) in Table 1.

© Toyota Central R&D Labs., Inc. 2017

formation of the staging structure in the Li-graphite intercalation compounds (Li-GICs). Using the hybrid QM-CL simulation method, the diffusion processes of Li ions with the interaction between Li ions have been analyzed. In this simulation, the stress field created by the deformation of C layers in the Li-GICs are taken into consideration. The hybrid QM-CL simulation method can accurately deal with a largescale system involved chemical reactions such as the formation process of the SEI in the LIBs.

The constant-current discharge properties of polycrystalline $LiCoO_2$ were theoretically investigated in relation to the grain size, the spatial distribution of the crystal orientation of each grain, the grain-boundary diffusivity, and the elastic strain energy. A Li-diffusion model that takes into account the elastic strain energy was developed for $LiCoO_2$. This model confirmed that the effect of a stress field on the apparent diffusion coefficient of Li varied according to the relationship between the crystallographic orientation and the direction of Li diffusion. The elastic strain energy, which was varied according to the Li intercalation, also exhibited a non-negligible effect on the discharge properties. The relationship between various microstructural features and the constant-current discharge properties of $LiCoO_2$ was presented. The discharge capacity of $LiCoO_2$ at a high discharge rate (e.g., 20C) was affected by the microstructure, namely the grain size, the spatial distribution of crystal orientations for each grain, and the GB diffusivity throughout the apparent Li diffusivity. The calculated results suggest that both the intergranular angle mismatch and the GB diffusivity are crucial parameters for evaluating the apparent discharge property.

Acknowledgements

We thank Prof. Shuji Ogata, Nagoya Institute of Technology, Prof. Toshiyuki Koyama, Nagoya University, and Dr. Hisatsugu Yamasaki, Toyota Motor Corp., from whom we received substantial help and insightful comments. The research in Sec. 2 is supported by MEXT Strategic Programs for Innovative Research (SPIRE), the Computational Materials Science Initiative (CMSI), the High Performance Computing Infrastructure (HPCI) of RIST (hp120123, hp13022, hp140096, hp140214, hp150041), and a Grant-in-Aid for Scientific Research (Kakenhi: 23310074) of Japan. The computations were performed using the K computer at AICS of RIKEN, a Fujitsu FX10 at the Information Technology Center of University of Tokyo, a Fujitsu FX10 at the Institute for Solid State Physics of the University of Tokyo, a Hitachi SR16000 at the Institute for Materials Research of Tohoku University, a Fujitsu FX1 and an FX10 at the Information Technology Center of Nagoya University, and a Fujitsu PRIMERGY at the Research Center for Computational Science (Okazaki).

References

(1) Bordin, O. and Smith G. D., *J. Phys. Chem. B*, Vol. 113, No. 6 (2009), pp. 1763-1776.
(2) Ogata, S., Lidorikis, E., Shimojo, F., Nakano, A., Vashishta, P. and Kalia, R. K., *Comput. Phys. Commun.*, Vol. 138, No. 2 (2001), pp. 143-154.
(3) Ogata, S., Shimojo, F., Kalia, R. K., Nakano, A. and Vashishta, P., *Comput. Phys. Commun.*, Vol. 149, No. 1 (2002), pp. 30-38.
(4) Ogata, S., *Phys. Rev. B*, Vol. 72, No. 4 (2005), 045348.
(5) Ohba, N., Ogata, T., Tamura, T., Yamakawa, S. and Asahi, R., *Comput. Model. Eng. Sci.*, Vol. 75, No. 4 (2011), pp. 247-266.
(6) Ohba, N., Ogata, S., Tamura, T., Kobayashi, R., Yamakawa, S. and Asahi, R., *J. Phys. Soc. Jpn.*, Vol. 81 (2012), No. 023601.
(7) Ohba, N., Ogata, S., Kouno, T., Tamura, T. and Kobayashi, R., *Comput. Phys. Commun.*, Vol. 183, No. 8 (2012), pp. 1664-1673.
(8) Ogata, S., Ohba, N. and Kouno, T., *J. Phys. Chem. C*, Vol. 117, No. 35 (2013), pp. 17960-17968.
(9) Eichinger, M., Tavan, P., Hutter, J. and Parrinello, M., *J. Chem. Phys.*, Vol. 110, No. 21 (1999), 10452.
(10) Brenner, D. W., *Phys. Rev. B*, Vol. 42 (1990), No. 15, Article No. 9458.
(11) Brenner, D. W., *Phys. Rev. B*, Vol. 46 (1992), No. 3, Article No. 1948.
(12) Shimojo, F., Campbell, T. J., Kalia, R. K., Nakano A., Vashishta, P., Ogata, S. and Tsuruta, K., *Future Gener. Comput. Syst.*, Vol. 17, No. 3 (2000), pp. 279-291.
(13) Ohba, N., Ogata, S., Kouno, T. and Asahi, R., *Comput. Mater. Sci.*, Vol. 108, Part A (2015), pp. 250-257.
(14) Mizushima, K., Jones, P., Wiseman, P. and Goodenough, J. B., *Mater. Res. Bull.*, Vol. 15, No. 6 (1980), pp. 783-789.
(15) Plichta, E., Salomon, M., Slane, S., Uchiyama, M., Chua, D., Ebner, W. and Lin, H., *J. Power Sources*, Vol. 21, No. 1 (1987), pp. 25-31.
(16) Auborn, J. and Barberio, Y., *J. Electrochem. Soc.*, Vol. 134, No. 3 (1987), pp. 638-641.
(17) Antoline, E., *Solid State Ionics*, Vol. 170, No. 3-4 (2004), pp. 159-171.

© Toyota Central R&D Labs., Inc. 2017

(18) Scrosati, B. And Garche, J., *J. Power Sources*, Vol. 195, No. 9 (2010), pp. 2419-2430.
(19) Wang, X., Loa, I., Kunc, K., Syassen, K. and Amboage, M., *Phys. Rev. B*, Vol. 72, No. 22 (2005), 224102.
(20) Xie, J., Imanichi, N., Matsumura, T., Hirano, A., Takeda, Y. and Yamamoto, O., *Solid State Ionics*, Vol. 179, No. 9-10 (2008), pp. 362-370.
(21) Fisher, C., Huang, R., Hitosugi, T., Moriwake, H., Kuwabara, A., Ikuhara, Y. H., Oki, H. and Ikuhara, Y., *Nanosci. Nanotechnol. Lett.*, Vol. 4, No. 2 (2012), pp. 165-168.
(22) Christensen, J., and Newman, J., *J. Electrochem. Soc.*, Vol. 153, No. 6 (2006), pp. A1019-A1030.
(23) Renganathan, S., Sikha, G., Santhanagopalan, S. and White, R. E., *J. Electrochem. Soc.*, Vol. 157, No. 2 (2010), pp. A155-A163.
(24) Yamakawa, Y., Yamasaki, H., Koyama, T. and Asahi, R., *J. Power Sources*, Vol. 223, No. 1 (2013), pp. 199-205.
(25) Yamakawa, S., Yamasaki, H., Koyama, T., Asahi, R., *Solid State Ionics*, Vol. 262 (2014), pp. 56-60.
(26) Tarascon, J. -M. and Armand, M., *Nature*, Vol. 414 (2001), pp. 359-367.
(27) Wang, Y. U., Jin, Y. M. and Khacaturyan, A. G., J. *Appl. Phys.*, Vol. 91, No. 10 (2002), pp. 6435-6451.
(28) Hu, S. and Chen, L., *Acta Mater.*, Vol. 49, No. 11 (2001), pp. 1879-1890.
(29) Van der Ven, A., Ceder, G., Asta, M. and Tepesch, P., *Phys. Rev. B*, Vol. 64, No. 18 (2001), 184307.
(30) Kim, S. G., Kim, D. I., Kim, W. T. and Park, Y. B., *Phys. Rev. E*, Vol. 74, No. 6 (2006), 061605.
(31) Hart, F. and Bates, J., *J. Appl. Phys.*, Vol. 83, No. 12 (1998), pp. 7560-7566.
(32) Van der Ven, A., Aydinol, M., Ceder, G., Kresse, G. and Hafner, *J., Phys. Rev. B*, Vol. 58, No. 6 (1998), Article No. 2975.
(33) Takahashi, Y., Kijima, N., Tokiwa, K., Watanabe, T. and Akimoto, *J. Phys.: Condens. Matter*, Vol. 19, No. 43 (2007), 436202.
(34) Takahashi, Y., Kijima, N., Dokko, K., Nishizawa, M., Uchida, I. and Akimoto, J., *J. Solid State Chem.*, Vol. 180, No. 1 (2007), pp. 313-321.
(35) Zhang, Q., Guo, Q. and White, R. E., *J. Electrochem. Soc.*, Vol. 153, No. 2 (2006), pp. A301-A309.
(36) Pyun, S. -I., Go, J. -Y., Jang, T. -S., *Electrochim. Acta*, Vol. 49, No. 25 (2004), pp. 4477-4486.
(37) Wen, C. J., Boukamp, B., Huggins, R. and Weppner, W., *J. Electrochem. Soc.*, Vol. 126, No. 12 (1979), pp. 2258-2266.

Fig. 11
Reprinted from J. Power Sources, Vol. 233 (2013), pp. 199-205, Yamakawa, S., Yamasaki, H., Koyama, T. and Asahi, R., Numerical Study of Li Diffusion in Polycrystalline $LiCoO_2$, © 2013 Elsevier, with permission from Elsevier.

Figs. 12, 14, 15 and Table 1
Reprinted from Solid State Ionics, Vol. 262 (2014), pp. 56-60, Yamakawa, S., Yamasaki, H., Koyama, T. and Asahi, R., Effect of Microstructure on Discharge Properties of Polycrystalline $LiCoO_2$, © 2014 Elsevier, with permission from Elsevier.

Nobuko Ohba
Research Fields:
- Computational Materials Science
- First-principles Calculations for Solid Materials
- Materials Infomatics

Academic Degree: Dr.Eng.
Academic Societies:
- The Physical Society of Japan
- American Physical Society
- The Japan Institute of Metals and Materials
- The Japan Society of Mechanical Engineers

Award:
- Certificate of Merit for Best Technological Presentation, JSME 22nd Computational Mechanics Division Conference, 2009

Shunsuke Yamakawa
Research Field:
- Computational Materials Science

Academic Degree: Dr.Eng.
Academic Society:
- The Japan Institute of Metals and Materials

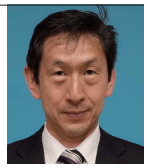

Ryoji Asahi
Research Field:
- Computational Materials Design for Development of Functional Materials

Academic Degree: Ph.D.
Academic Societies:
- The Japan Society of Applied Physics
- The Japan Institute of Metals
- American Physical Society

Award:
- Technical Development Award, the Chemical Society of Japan, 2006

© Toyota Central R&D Labs., Inc. 2017